# Robust Supervised Method for Nonlinear Spectral Unmixing Accounting for Endmember Variability

Bikram Koirala, *Graduate Student Member, IEEE*, Zohreh Zahiri, *Member, IEEE*, Alfredo Lamberti, and Paul Scheunders, *Senior Member, IEEE*

***Abstract*— Due to the complex interaction of light with mixed materials, reflectance spectra are highly nonlinearly related to the pure material endmember spectra, making it hard to estimate the fractional abundances of the materials. Changing illumination conditions and cross-sensor situations cause spectral variability, further complicating the unmixing procedure. In this work, we propose a supervised approach to unmix mineral powder mixtures, containing endmember variability. First, the abundances are estimated by calculating the geodesic distances between the mixtures and the endmembers. It is argued and experimentally validated that the estimated geodesic abundances, although not correct, are invariant to external spectral variability. Then, a supervised approach is applied to learn a mapping from the obtained geodesic abundances to spectra that follow a linear model. To learn this mapping, groundtruth fractional abundances of a number of training samples are required. Although any nonlinear regression method can be used to learn the mapping, Gaussian process is found to be suitable when a limited number of training samples are available. The trained model is applicable to all manifolds that contain a similar nonlinear behavior as the trained manifold, e.g., when the same mixtures are measured by another sensor. Using the output spectra, a simple inversion of the linear model reveals the true abundances. Experiments are conducted on simulated and real mineral mixtures. In particular, we developed data sets of homogeneously mixed mineral powder mixtures, acquired by two different sensors, an Agrispec spectrometer and a snapscan shortwave infrared (SWIR) hyperspectral camera, under strictly controlled experimental settings. The proposed approach is compared to other supervised approaches and nonlinear mixture models.**

***Index Terms*— Hyperspectral, machine learning regression, mineral powder mixtures, mixing models.**

## I. Introduction

THE goal of spectral unmixing is to estimate the fractional abundances of the different pure materials (endmembers) that are contained within a hyperspectral pixel. Generally, spectral unmixing is performed by defining a mathematical model that describes the spectral reflectance as a function of the endmembers and their fractional abundances. The inversion of that model then gives an estimation of the pixels composition.

Among all mathematical models, the linear mixing model (LMM) [1] is the most popular one. This model assumes that each incoming ray of light interacts only once with a specific pure material in the pixel before reaching the sensor. When taking into account the physical nonnegativity and sum-to-one constraints of the fractional abundances, the fully constrained least squares unmixing (FCLSU) [2], [3] procedure can be applied to minimize the error between the true and the reconstructed spectrum.

The LMM produces large errors when the hyperspectral data set is obtained from complex geometrical structures or intimate mixtures. In these scenarios, the incident ray of light interacts with several pure materials within a hyperspectral pixel before reaching the sensor. There exist several nonlinear mixing models that model multiple interactions [4]. The bilinear models ( [4], [5]) extend the LMM by adding bilinear terms, allowing the incident ray to interact with two pure materials before reaching the sensor. Other models extend these toward multiple interactions, e.g., the multilinear mixing model (MLM) [6] and the $p$-linear ($p > 2$) mixing model (pLMM) [7]–[9].

The most advanced nonlinear mixing models are physics-based radiative transfer models. These models are often employed for modeling intimate mixtures of materials. They represent the medium as a half-space filled with particles with known densities and distributions of physical attributes. The Hapke model is a simplified version of a radiative transfer model and was developed to explain the interaction of the light with intimately mixed materials [10], [11].

Instead of depending on a particular mixing model for spectral unmixing, some attempts have been made to learn the nonlinearity of the data set using a data-driven approach. Algorithms were developed that performed the spectral unmixing in a reproducing kernel Hilbert space [12], [13]. Radial basis function kernels were used to kernelize FCLSU (KFCLS), but no improvement in the unmixing of intimate mixtures was observed [14], [15].

Supervised spectral unmixing methods were developed that require groundtruth fractional abundances of a number of training spectra [16]–[20]. These methods apply the ground truth as training data to learn the nonlinear relationship between the measured spectra and the fractional abundances.

Manuscript received August 11, 2020; revised September 30, 2020; accepted October 8, 2020. This work was supported by the Belgian Science Policy Office (BELSPO) in the frame of the STEREO III Program-Project GEOMIX under Grant SR/06/357. *(Corresponding author: Bikram Koirala.)*

Bikram Koirala, Zohreh Zahiri, and Paul Scheunders are with the Imec-Vision Laboratory, Department of Physics, University of Antwerp, 2610 Antwerp, Belgium (e-mail: bikram.koirala@uantwerpen.be; zohreh.zahiri@uantwerpen.be; paul.scheunders@uantwerpen.be).

Alfredo Lamberti is with ENGIE Laborelec, 1630 Linkebeek, Belgium (e-mail: alfredo.lamberti@engie.com).

Color versions of one or more of the figures in this article are available online at http://ieeexplore.ieee.org.

Digital Object Identifier 10.1109/TGRS.2020.3031012

One disadvantage is that a direct mapping to the abundances is unconstrained and does not guarantee that the obtained results correspond to the actual fractions. To solve this issue, in [21] and [22], a mapping of the nonlinear spectra to the linear model was learned with machine learning regression algorithms, after which FCLSU was applied to estimate the fractional abundances.

A major disadvantage of the supervised methods is their generalizability. When the training and test samples lie on different data manifolds, the performance of this methodology decreases. This occurs in any situation containing spectral variability. There exist several algorithms that consider endmember variability, that can be separated into two groups: methods based on endmember bundles and methods that apply physical and statistical models ([23]–[25]). The first group of algorithms defines a set of multiple spectral signatures (endmember bundles) to characterize each endmember class ([26]). Endmember bundles can be extracted from the hyperspectral image (HSI) by applying endmember bundle extraction methods ( [27]–[29]). In [30], it is pointed out that endmember bundles cannot completely represent all endmember variability in HSIs. The second group of algorithms tackles spectral variability either by incorporating additional variability terms in the LMM ([31]–[33]) or relies on a statistical representation of the endmembers ( [34]–[36]). In [37], an algorithm is developed that bridges the gap between endmember bundle-based methods and parametric physics-based models. In [38], spectral variability was treated as a denoising problem. All these methods however were developed for linearly mixed data sets. The situation is much more complex when the endmembers are mixed nonlinearly.

There exist different types of spectral variability. External spectral variability may be caused by variable acquisition conditions, i.e., variable illumination conditions, distance, and orientation from the sensor [39]. These effects cause a (global or pixel-based) scaling of the spectral reflectance. Although the intrinsic nonlinearity of the data manifold does not change with scaling, nonlinear mixing models are not invariant to scaling, since the spectral reflectance is a nonlinear function of the endmembers and fractional abundances.

Another type of external variability may occur between different data sets, e.g., obtained from different sensors, or when different white calibration panels are used. These effects cause a wavelength dependent variation of the spectra, for which nonlinear models are not invariant. However, since the intrinsic physics is the same, the data manifolds have the same nonlinear behavior.

Intrinsic spectral variability occurs when the material composition changes from one mixture to another, e.g., caused by variable grain size distributions. This is expected to change the nonlinear behavior of the manifold. In this work, intrinsic variability is assumed to be absent and is not considered.

The literature reports only limited research devoted to the treatment of spectral variability in relation to nonlinear unmixing. Drumetz *et al.* [40] proposed a band-wise scaling of the LMM to model either spectral variability in the linear case or nonlinear mixing. In [41] and [42], bilinear models were extended with a scaling term to tackle external spectral variability. In [43], endmembers were modeled by a normal distribution to reduce the influence of endmember variability in bilinear models. In [44], a neighbor-band ratio unmixing (NBRU) approach was introduced to estimate fractional abundances from mineral mixtures, and its robustness against endmember variability was validated. In [45], a multitype mixing model was proposed to handle nonlinear unmixing and spectral variability for the purpose of HSI reconstruction.

In general, inversion of a model that treats spectral variability and nonlinearity simultaneously is highly nonconvex. Most of the proposed models have large amounts of hyperparameters, making an abundance estimation hard. Moreover, relying on one particular model makes a method inflexible in, e.g., cross-sensor situations.

In this work, we will develop a supervised model-independent approach to handle spectral variability for nonlinear unmixing. The method uses a geodesic distance-based unmixing approach [46]. This approach can be shown to be invariant to external spectral variability, and to estimate the same abundances on data manifolds with the same underlying nonlinear behavior. However, only for manifolds with constant curvature, the estimated abundances are correct. This is unfortunately not the case in nonlinearly mixed data, for which the geodesic distance is nonlinearly related to the fractional abundance. For this, the approach is combined with a supervised nonlinear regression method, to learn the nonlinear relationship between the abundances, estimated by the geodesic approach and the actual ones.

The major disadvantage of supervised methods is that they require groundtruth data in the form of endmembers as well as fractional abundances. Very limited research has been devoted to producing ground truth data for spectral unmixing tasks [47]. Most of the spectral unmixing tasks are focused on estimating fractional abundances from airborne or satellite HSIs. To produce unmixing groundtruth data for these images is difficult. This restricts the validation of the developed algorithms on real data sets to visual interpretations.

Recent developments in compact, low-cost hyperspectral sensors, allow us to produce hyperspectral data sets in laboratory settings. To validate our strategy, we produced a hyperspectral data set of mineral powder mixtures. To include spectral variability, we acquired the spectra by two different sensors: an Agrispec spectrometer and a snapscan shortwave infrared (SWIR) hyperspectral camera. Both the images/spectra of pure minerals and their mixtures are available. To the best of our knowledge, this data set is the first publicly available data set captured by two independent sensors. Experiments on the Relab mineral mixture data set will also be performed.

The remaining of this article is organized as follows: Section II is devoted to prior work. We introduce some of the nonlinear mixing models, the geodesic unmixing (GU) approach and the supervised nonlinear unmixing approaches. In Section III, the proposed methodology is elaborated. In Section IV, we describe the self-crafted and Reflectance Experiment Laboratory (RELAB) mineral mixture data sets on which our methodology is validated. In Section V, we describe the experiments and the results, followed by a discussion in Section VI. Section VII concludes this work.

## II. Relevant Prior Work

### A. Hyperspectral Mixing Models

In this section, we first fix some notation and describe a few mixing models. Let $\mathbf{E}(\{\mathbf{e}_j\}_{j=1}^{p} \in \mathbf{R}_+^d)$ be a set of $p$ endmembers (i.e., pure spectra) composed of $d$ spectral bands. Suppose that $N$ samples contain mixtures of these endmembers, with fractional abundances denoted by the matrix $\mathbf{A}(\{\mathbf{a}_i\}_{i=1}^{N} \in \mathbf{R}_+^p)$. It is generally assumed that the spectral reflectances of these $N$ samples, $\mathbf{Y}(\{\mathbf{y}_i\}_{i=1}^{N} \in \mathbf{R}_+^d)$ are generated by a nonlinear function $F$ of the endmembers and fractional abundances

$$\mathbf{y}_i = F(\mathbf{E}, \mathbf{a}_i) + \boldsymbol{\eta}_i \tag{1}$$

where $\boldsymbol{\eta}_i$ represents Gaussian noise. Each mixing model corresponds to a particular choice of $F$.

*1) Linear Mixing Model:* The LMM assumes that $\mathbf{Y}$ is given by

$$\mathbf{Y} = \mathbf{EA} + \mathbf{N} \tag{2}$$

where $\mathbf{N}$ represents the matrix containing gaussian noise. When assuming that the fractional abundances are nonnegative and sum-to-one, the FCLSU algorithm estimates the fractional abundances by minimizing $\|\mathbf{y}_i - \mathbf{E}\mathbf{a}_i\|^2$ s.t. $\sum_j a_{ji} = 1$, $\forall j : a_{ji} \geq 0$.

*2) Bilinear Mixing Models:* Bilinear models have been designed to allow for secondary reflections. In [5], the Fan model is derived by the first-order Taylor series expansion of a general nonlinear mixing function

$$\begin{aligned}\mathbf{y}_i &= F(\mathbf{E}, \mathbf{a}_i) + \boldsymbol{\eta}_i \\ &= \mathbf{E}\mathbf{a}_i + \sum_{j=1}^{p-1} \sum_{k=j+1}^{p} a_{ji} a_{ki} \mathbf{e}_j \odot \mathbf{e}_k + \boldsymbol{\eta}_i\end{aligned} \tag{3}$$

where $\odot$ is the elementwise multiplication of two vectors. The main disadvantage of the Fan model is that its performance on linearly mixed data is very low. To generalize the bilinear models to the linear case, the generalized bilinear model (GBM) ([48]), the polynomial post nonlinear mixing model (PPNMM) ([49]) and the linear quadratic model (LQM) ([4]) are developed. Although bilinear models can explain second-order reflections, the main problem is that they allow hyperspectral pixels to have values outside of the range [0, 1].

*3) Multilinear Mixing Models:* Some recent models also consider higher-order reflections, e.g., the MLM, [6] and the $p$-linear ($p > 2$) mixture model (pLMM) [7]–[9].

*4) Hapke Model:* The Hapke model [10], [11] describes the optical characteristics of intimately mixed materials. This model assumes that the particles have a size, much larger than the wavelength of the light, are of similar shape, and are randomly oriented. In general, this model requires information regarding the physical state of the surface (particle size, surface roughness, etc.), the real and imaginary parts of the optical indexes, and the viewing geometry. In [50], it was simplified for remote sensing applications. This simplified version of the Hapke model relates the bidirectional reflectance $\mathbf{Y}$ with the single scattering albedos (SSA) $\mathbf{W}(\{\mathbf{w}_i\}_{i=1}^{N} \in \mathbf{R}_+^d)$ by the following equation:

$$\begin{aligned}\mathbf{Y} &= F(\mathbf{E}, \mathbf{A}) \\ &= \frac{\mathbf{W}}{(1 + 2\mu\sqrt{1 - \mathbf{W}})(1 + 2\mu_0\sqrt{1 - \mathbf{W}})}\end{aligned} \tag{4}$$

where $\mu = \cos(\theta_e)$ and $\mu_0 = \cos(\theta_i)$ are the cosines of the angles with the normal of the outgoing and incoming radiation, respectively. While the reflectance of intimately mixed materials does not follow the LMM, the SSA do follow it:

$$\mathbf{w}_i = \mathbf{W}^{\mathbf{E}}\mathbf{a}_i \tag{5}$$

where $\mathbf{W}^{\mathbf{E}}(\{\mathbf{w}_j^{\mathbf{E}}\}_{j=1}^{p} \in \mathbf{R}_+^d)$ denotes the SSA of the endmembers.

### B. Geodesic Unmixing

Following a geometric description of the LMM, the data manifold is a simplex, spanned by the endmembers which form a linear basis for the mixed pixel spectra. Many unmixing algorithms exploit this geometric notion. With this description, the spectral unmixing can be described in a distance-based manner, in which the fractional abundances $a_j$ of a data point $\mathbf{y}$ can be written as

$$a_j = \frac{\mathrm{V}(\mathbf{e_1}, \ldots, \mathbf{y}, \mathbf{e}_{j+1}, \ldots, \mathbf{e}_p)}{\mathrm{V}(\mathbf{e_1}, \ldots, \mathbf{e}_p)} \tag{6}$$

i.e., the volume of the simplex obtained by replacing the $j$th vertex by $\mathbf{y}$, divided by the total volume of the largest simplex. The volume of a simplex is calculated as

$$\mathrm{V}\ (\mathbf{e_1}, \ldots, \mathbf{e_p}) = \sqrt{\frac{(-1)^p \cdot\ \mathrm{cmd}\ (\mathbf{E})}{2^{p-1}(p-1)!}}$$

with

$$\mathrm{cmd}\ (\mathbf{E}) = \det \begin{pmatrix} 0 & 1 & 1 & 1 & \ldots & 1 \\ 1 & 0 & d_{1,2}^2 & d_{1,3}^2 & \ldots & d_{1,p}^2 \\ 1 & d_{2,1}^2 & 0 & d_{2,3}^2 & \ldots & d_{2,p}^2 \\ 1 & d_{3,1}^2 & d_{3,2}^2 & 0 & \ldots & d_{3,p}^2 \\ \vdots & \vdots & \vdots & \vdots & \ddots & \vdots \\ 1 & d_{p,1}^2 & d_{p,2}^2 & d_{p,3}^2 & \ldots & 0 \end{pmatrix} \tag{7}$$

where cmd denotes the Cayley–Menger determinant and $d_{m,k}^2$ is the (Euclidean) distance between endmembers $\mathbf{e}_m$ and $\mathbf{e}_k$.

In [46], this geometric concept was extended to nonlinear manifolds, where the Euclidean distance can be replaced by the geodesic distance (see Fig. 1). A well-known data-driven approach for approximating geodesic distances on a manifold is the construction of a nearest neighbor graph on the data. The geodesic distance between any two points is then defined as the shortest-path distance along the graph (i.e., using locally the Euclidean distance between neighboring points on the graph) between these two points. The Dijkstra algorithm [51] can be used to calculate the shortest-path distances. These distances approximate the true geodesic distances as measured along the surface of the data manifold.

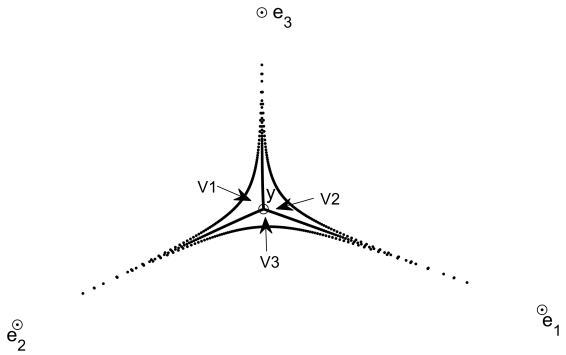


Fig. 1. Data point $\mathbf{y}$ lies inside the nonlinear simplex spanned by $\mathbf{e_1}, \mathbf{e_2}, \mathbf{e_3}$. The fractional abundance $a_j$ is equal to the volume ratio $\mathrm{V}_j/\mathrm{V}$, with $\mathrm{V} = \sum_j \mathrm{V}_j$.

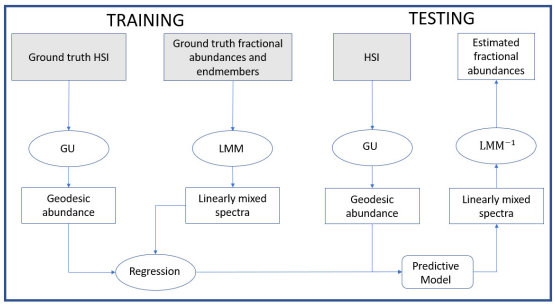


Fig. 2. Flowchart of the proposed method.

### C. Supervised Approaches for Nonlinear Spectral Unmixing

With most of the nonlinear mixing models, it is hard to physically interpret the estimated parameters and link them to the actual fractional abundances. For this reason, supervised approaches were developed to learn the nonlinear relationship between the spectral reflectance and the fractional abundances [16]–[20]. A prerequisite is the availability of a training set of nonlinearly mixed spectral reflectances and groundtruth information about their endmembers and fractional abundances. These methods learn a direct mapping from the hyperspectral data to the fractional abundances, and in this way, do not comply with the physical positivity and sum-to-one constraints.

In [22], we proposed a strategy to solve these issues. In the proposed method, from the available training data, linearly mixed spectra were generated. Then, a map between the actual training spectra and the generated linear spectra was learned by a nonlinear regression technique. Finally, the unknown spectra are mapped using the learned regression model and the FCLSU technique is applied to estimate the fractional abundances of the mapped spectra.

The main disadvantage of the supervised approaches is that the performance decreases when the training and test samples are from different data manifolds, caused by external spectral variability, e.g., when the training and test samples are captured by two independent sensors, or when the illumination conditions on the training and the test samples are not entirely similar.

## III. Supervised Geodesic Unmixing (GSU)

In this work, we propose a supervised nonlinear unmixing approach in which the external spectral variability is fully taken into account by a combination of a supervised mapping procedure with the GU approach. Fig. 2 illustrates the proposed methodology. We will refer to this approach as geodesic supervised unmixing (GSU).

### A. Step 1: Geodesic Unmixing

In a first step, the GU approach is applied to calculate the geodesic fractional abundances. Let us focus on binary mixtures from now on. The manifold, sampled by a number of binary mixtures of two materials is a curve in spectral space between the two endmembers. The curve can be approximated by a piecewise linear curve and the geodesic distance is then simply approximated by the sum of the Euclidean distances between neighboring samples on the 1-neural network (NN) graph. For this, it is important to correctly order these samples. This is done by generating a distance matrix, containing the distances from each point to any other point, starting from an endmember and iteratively looking for the next closest point. The more mixture samples are available, the better the approximation. In some practical situations, only one mixture (and the two endmembers) may be available, so that the approximation leads to errors. However, since the degree of the manifold curves is expected to be low, the errors are limited to a few percent.

For the geodesic distance to lead to the correct fractional abundances, the data manifold should have a small nonzero constant curvature. In that case, the arc length between the endmembers and the mixture along the manifold is proportional to the fractional abundance. This is the case, e.g., for a circle and a helix, but not so for a parabola. It is very unlikely that a real data manifold will satisfy this condition. The fractional abundances estimated by GU for data sets generated by the bilinear models or the Hapke model have a nonlinear relationship with the true fractional abundances. In Appendix A, this is illustrated for the Fan model.

To further demonstrate this, we simulated a data manifold of binary mixtures of Bronzite and Calcite, for which the endmember spectra are obtained by the United States Geological Survey (USGS) library [Fig. 3(a)]. The groundtruth fractional abundances were generated uniformly from the unit simplex and mixtures were simulated according to the Hapke model. In Fig. 3(c), the true fractional abundance is plotted against the estimated fractional abundance by GU.

Despite the fact that the geodesic distance-based unmixing produces large errors in estimating fractional abundances of nonlinear hyperspectral data sets, the main advantage of this approach is that it is invariant to external variability. To illustrate this, we scale the Bronzite–Calcite manifold [Fig. 3(b)] and again plot the estimated against the true abundances [Fig. 3(c)]. As can be observed, the estimated geodesic abundances remain invariant. Nonlinear models however are not invariant to such scaling. To demonstrate this, Fig. 3(b) shows that the data manifolds, generated by the Hapke model from

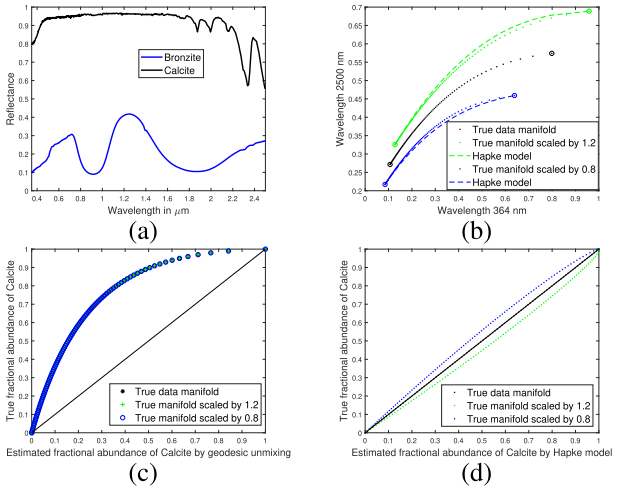


Fig. 3. (a) Endmember spectra of Bronzite and Calcite. (b) True data manifold and scaled versions. The dashed lines represent the data manifold, generated by the Hapke model. (c) True fractional abundance of Calcite against the one estimated by GU. (d) True fractional abundance of Calcite against the one estimated by the Hapke model.

the scaled endmembers do not follow the scaled manifold. Fig. 3(d) plots the obtained abundances by Hapke against the true ones. As can be observed, the performance of the Hapke model for estimating the fractional abundances drops significantly on the scaled manifolds. This demonstrates that the geodesic distance approach produces incorrect abundances but is able to reveal the underlying nonlinearities, which remain the same after global scaling the manifold. In the experimental validation, we will extend this claim to more general external wavelength-dependent variability caused by cross-sensor differences and propose a method to deal with random spectral variability of individual samples.

To summarize: GU produces identical fractional abundances on manifolds in which the underlying nonlinearity is the same. The estimated geodesic fractional abundances $(\hat{\mathbf{A}}(\{\hat{\mathbf{a}}_i\}_{i=1}^N \in \mathbf{R}_+^p))$ are incorrect and are nonlinearly related to the true fractional abundances.

### *B. Step 2: Supervised Mapping*

In order to derive the correct abundances from the estimated ones by GU, we will resort to a supervised approach. To this aim, we assume that a set of $n$ training samples with known fractional abundances: $\mathcal{D} = \{(\mathbf{y}_1, \mathbf{a}_1), \ldots, (\mathbf{y}_n, \mathbf{a}_n)\}$ is available. One approach would be to learn a direct mapping from the estimated geodesic abundances to the actual abundances. This would however not automatically account for the abundance sum-to-one and positivity constraints. For this, we propose a method that learns a mapping from the geodesic abundances to linearly mixed spectra.

First, linearly mixed spectra are generated from the endmembers and their fractional abundances from the available training data

$$\mathbf{x}_i = \mathbf{E}\mathbf{a}_i \quad \forall i \in \{1, \ldots, n\}. \tag{8}$$

Then, a map is learned from the estimated geodesic abundances of the training set $\hat{\mathbf{A}}_\mathcal{D} = \{\hat{\mathbf{a}}_i\}_{i=1}^n$ to the generated linearly mixed spectra $\mathbf{X}_\mathcal{D}$. Any nonlinear regression method may be applied to train such a model. In this work, we choose Gaussian Processes regression [52].

A GP [52] learns the nonlinear relationship between the input abundances $\hat{\mathbf{A}}_\mathcal{D}$ and output spectra $\mathbf{X}_\mathcal{D}$ as a Bayesian regression, by estimating the distribution of mapping functions that are coherent with the training set. It is assumed that the observed output variables $(\mathbf{x}_i)$ can be described in function of the input $(\hat{\mathbf{a}}_i)$ by

$$\mathbf{x}_i = f(\hat{\mathbf{a}}_i) = \boldsymbol{\phi}(\hat{\mathbf{a}}_i)^T \mathbf{w} \tag{9}$$

with prior $\mathbf{w} \sim \mathcal{N}(\mathbf{0}, \Sigma_p)$. The function $\phi(\cdot)$ maps the input to an infinite-dimensional feature space. The mean and covariance of the outputs are given by

$$\begin{aligned} \mathbb{E}[f(\hat{\mathbf{a}}_i)] &= \boldsymbol{\phi}(\hat{\mathbf{a}}_i)^T \mathbb{E}[\mathbf{w}] = \mathbf{0} \\ \mathbb{E}[f(\hat{\mathbf{a}}_i) f(\hat{\mathbf{a}}_j)] &= \boldsymbol{\phi}(\hat{\mathbf{a}}_i)^T \mathbb{E}[\mathbf{w}\mathbf{w}^T] \boldsymbol{\phi}(\hat{\mathbf{a}}_j) = \boldsymbol{\phi}(\hat{\mathbf{a}}_i)^T \Sigma_p \boldsymbol{\phi}(\hat{\mathbf{a}}_j). \end{aligned} \tag{10}$$

GP assumes that the covariance of the outputs can be modeled by the squared exponential kernel function

$$\boldsymbol{\phi}(\hat{\mathbf{a}}_i)^T \Sigma_p \boldsymbol{\phi}(\hat{\mathbf{a}}_j) = k(\hat{\mathbf{a}}_i, \hat{\mathbf{a}}_j) = \sigma_f^2 \exp\left( -\sum_{b=1}^{p} \frac{(\hat{a}_i^b - \hat{a}_j^b)^2}{2 l_b^2} \right) \tag{11}$$

where $\sigma_f^2$ is the variance of the input abundances, and $l_b$ is a characteristic length-scale for each endmember. The joint distribution of the training output $(\mathbf{X}_\mathcal{D})$ and the test output $(f(\hat{\mathbf{A}}_t))$ can then be written as follows:

$$\begin{aligned} & p\left(f\left(\hat{\mathbf{A}}_t^T\right), \mathbf{X}_\mathcal{D}^T\right) \\ & \quad \sim \mathcal{N}\left(\mathbf{0}, \begin{bmatrix} K(\hat{\mathbf{A}}_t, \hat{\mathbf{A}}_t) & K(\hat{\mathbf{A}}_t, \hat{\mathbf{A}}_\mathcal{D}) \\ K(\hat{\mathbf{A}}_\mathcal{D}, \hat{\mathbf{A}}_t) & K(\hat{\mathbf{A}}_\mathcal{D}, \hat{\mathbf{A}}_\mathcal{D}) + \sigma_n^2 \mathbf{I} \end{bmatrix}\right) \\ & \quad = \mathcal{N}\left(\mathbf{0}, \begin{bmatrix} \Sigma_{11} & \Sigma_{12} \\ \Sigma_{21} & \Sigma_{22} \end{bmatrix}\right) \end{aligned} \tag{12}$$

where $\sigma_n^2$ is the noise variance of the training abundances, $K(\hat{\mathbf{A}}_\mathcal{D}, \hat{\mathbf{A}}_t)$ is the matrix of kernel functions between the $n$ training samples and the test samples, and $K(\hat{\mathbf{A}}_t, \hat{\mathbf{A}}_t)$ is the matrix of kernel functions between the test samples. When using the partitioned inverse formula

$$\begin{aligned} & \begin{pmatrix} \Sigma_{11} & \Sigma_{12} \\ \Sigma_{21} & \Sigma_{22} \end{pmatrix}^{-1} \\ & \quad = \begin{pmatrix} \Sigma^{-1} & -\Sigma^{-1}\Sigma_{12}\Sigma_{22}^{-1} \\ -\Sigma_{22}^{-1}\Sigma_{21}\Sigma^{-1} & \Sigma_{22}^{-1} + \Sigma_{22}^{-1}\Sigma_{21}\Sigma^{-1}\Sigma_{12}\Sigma_{22}^{-1} \end{pmatrix} \end{aligned} \tag{13}$$

with $\Sigma = \Sigma_{11} - \Sigma_{12}\Sigma_{22}^{-1}\Sigma_{21}$, (12) can be factorized into the predictive distribution $p(f(\hat{\mathbf{A}}_t^T)|\mathbf{X}_\mathcal{D}^T)$ and the marginal $p(\mathbf{X}_\mathcal{D}^T)$

$$\begin{aligned} p\left(f\left(\hat{\mathbf{A}}_t^T\right), \mathbf{X}_\mathcal{D}^T\right) &= p\left(f\left(\hat{\mathbf{A}}_t^T\right)\middle|\mathbf{X}_\mathcal{D}^T\right) p\left(\mathbf{X}_\mathcal{D}^T\right) \\ &= \mathcal{N}\left(\Sigma_{12}\Sigma_{22}^{-1}\mathbf{X}_\mathcal{D}^T, \Sigma\right) \mathcal{N}(\mathbf{0}, \Sigma_{22}). \end{aligned} \tag{14}$$

The estimated map of the geodesic abundance $\hat{\mathbf{A}}_t$ to the linear spectra $\mathbf{X}_t$ is then given by

$$\begin{aligned} \mathbf{X}_t &= f(\hat{\mathbf{A}}_t) = \mathbf{X}_\mathcal{D}\Sigma_{22}^{-1}\Sigma_{12}^T \\ &= \mathbf{X}_\mathcal{D}\left(K(\hat{\mathbf{A}}_\mathcal{D}, \hat{\mathbf{A}}_\mathcal{D}) + \sigma_n^2 \mathbf{I}\right)^{-1} K(\hat{\mathbf{A}}_t, \hat{\mathbf{A}}_\mathcal{D})^T. \end{aligned} \tag{15}$$

TABLE I
DENSITY AND GRAIN SIZE (D50) OF THE MINERALS USED IN THE SELF-CRAFTED MINERAL DATA SET

| Mineral | Density ($g/cm^3$) | Grain size ($\mu m$) |
|---|---|---|
| $Al_2O_3$ | 3.98 | 3.5 |
| CaO | 3.34 | 2.7 |
| $Fe_2O_3$ | 5.26 | 0.8 |
| $SiO_2$ | 2.64 | 23 |
| $TiO_2$ | 3.89 | 0.5 |

The hyperparameters of the kernel function in (11) are optimized by minimizing the negative log marginal likelihood of the training data set ($-\log(p(\mathbf{X}_{\mathcal{D}}^T|\hat{\mathbf{A}}_{\mathcal{D}}^T))$).

### C. Step 3: Linear Unmixing

Once the mapping is learned and the test geodesic abundances are mapped onto the linear spectra, the final step is to obtain the fractional abundances from the mapped linear spectra, by inverting the LMM model. By learning a mapping to linear spectra, rather than learning a direct mapping between the geodesic abundances and the true abundances, the abundance constraints are automatically taken into account.

## IV. DATA

### A. Data Set 1: Self-Crafted Mineral Data Set

For the validation of our proposed method, we created a data set, containing in total 49 binary mixtures of mineral powders. The five chosen minerals are different oxides, typically found in soil, and applied in cementitious materials: Aluminum oxide ($Al_2O_3$), Calcium oxide (CaO), Iron oxide ($Fe_2O_3$), Silicon dioxide ($SiO_2$), and Titanium dioxide ($TiO_2$). The degree of purity of all minerals was above 98%. All mineral powders have a white color (except for Iron oxide which is red) and have different densities and grain sizes (see Table I).

In total, seven binary mixture combinations of minerals were prepared: $Al_2O_3$-$SiO_2$ (Al-Si), CaO-$SiO_2$ (Ca-Si), CaO-$TiO_2$ (Ca-Ti), $Fe_2O_3$-$Al_2O_3$ (Fe-Al), $Fe_2O_3$-CaO (Fe-Ca), $Fe_2O_3$-$SiO_2$ (Fe-Si) and $SiO_2$-$TiO_2$ (Si-Ti). For each mineral combination, seven different mixtures were prepared. We fixed the weight of each mixture to be in total 10 g (the scale had an accuracy of 0.001 g), and increased the weight of the first endmember in the mixture by a fixed step of 1.25 g, from 1.25 to 8.75 g. We then converted the weight to areal fraction, based on the known density and grain size of each pure material. For the case of tightly packed spherical particles, the areal fraction of each material can be written as follows:

$$a_j = \frac{\frac{M_j}{\rho_j D_j}}{\sum_{j=1}^{p} \frac{M_j}{\rho_j D_j}} \tag{16}$$

where $M_j$ is the mass fraction of component $j$, $\rho_j$ its density, and $D_j$ its average diameter.

Since the grain sizes and densities vary between the minerals, and the grain sizes are of the same order as the SWIR wavelength range, it can be expected that the Hapke model will not provide accurate areal fractional abundance estimates.

*1) Sample Preparation:* Before mixing the minerals, they were grinded to avoid clusters of grains causing inhomogeneities. The minerals were then put inside a glass container and mixed by rotating the container for approximately 5 min to guarantee a homogeneous mixture. Each mixture was then put inside a round black sample holder with an interior diameter of 20 mm, a height of 5.5 mm, and an edge thickness of approximately 3 mm. The sample holder was completely filled and compacted and smoothened using a stamp compactor. Each sample was scanned 3 times, each time emptying and refilling the sample holders.

The samples were scanned with two different instruments: a snapscan hyperspectral SWIR camera (manufactured by Imec) and an AgriSpec spectrometer [manufactured by Analytical Spectral Devices (ASD)].

*2) Scanning Setup of Hyperspectral Camera:* The spectral range of the camera is 1100–1670 nm with a spectral resolution of approximately 5 nm, resulting in a total of 113 spectral bands (the first 10 bands were very noisy and were discarded). In contrast to pushbroom systems, in which either the camera or the sample should move, in the snapscan camera the sensor moves inside the camera, allowing to acquire a still full image frame.

The samples were located in a region of 2 $cm^2$ in the center of the camera's field of view (FOV) to guarantee the lowest spectral variability. Four halogen lamps (20 W GU5.3 cool-fit) with diffusers were used for a hemispherical-directional illumination to simulate uniform real-world solar illumination. The distances of the sample to the halogens and the camera were approximately 30 and 40 cm, respectively. During scanning, the lights inside the room were turned off. Each image scan took approximately 45 s.

The original frame size of the raw images was 150 $\times$ 150 pixels. To provide data with uniform illumination and remove unrelated objects (edge of the sample holders) the images were clipped to 30 $\times$ 30 pixels. Since all mixtures were homogeneous, no spatial variation between the spectra was observed, and the spectra of all pixels were averaged over the entire clipped image.

*3) Scanning Setup of Spectrometer:* The data from the spectrometer have 1500 spectral bands, ranging from 1000 to 2500 nm with a step size of 1 nm. The wavelength range was clipped to the range of the hyperspectral camera, leaving 570 bands, from which the first 44 were noisy and discarded. The sensor is placed in a muglight for maximum illumination and sample stability, required for a good signal-to-noise ratio and to minimize measurement errors associated with stray light and specular reflected components. The muglight was mounted on top a box with a hole in the middle (slightly larger than the size of the sample holder), in order to place and remove the sample holders easily under the muglight. Every sample was individually held under the muglight for scanning from a fixed distance. The size of the scanning area in the spectrometer was 25 mm, thus positioning the edge of the sample holder in the FOV of the spectrometer. Since the spectrum of the sample holder was flat and close to zero in the entire spectral range of the spectrometer, this resulted in a slightly lower spectral reflectance. A slight horizontal

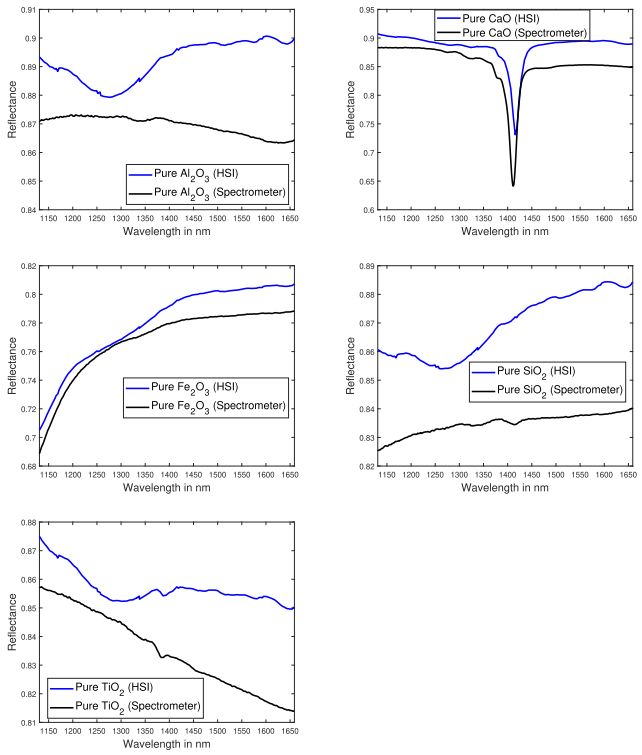


Fig. 4. Spectra of the pure minerals acquired by the spectrometer (black line) and hyperspectral camera (blue line).

degree of freedom resulted in a scaling effect on the acquired spectra. Three spectra were collected from each sample and by repeating the measurements 3 times (after emptying and refilling the sample holders), this resulted in nine spectra for each sample.

Fig. 4 shows the spectra of the pure materials acquired by both the spectrometer and the camera. A substantial difference between the acquired spectra can be observed, due to external variability, including variation in illumination and distance of the samples from the sensor, causing global scaling effects, and sensor-related differences, such as the use of different white-calibration, causing wavelength dependent scaling. Although we could correct for the latter, by applying the same calibration panel in both cases, we deliberately did not, to provoke cross-sensor differences.

The data set and the trained models generated by the proposed method on this data set are publicly available at "https://github.com/VisionlabUA/Mineral-dataset."

### *B. Data Set 2: RELAB Data Set*

This data set contains spectra of crafted mineral mixtures from the NASA RELAB at Brown University, publicly available at www.planetary.brown.edu/relab/ [53]. From the data set, binary mixtures from five minerals: Anorthite (An), Bronzite (Br), Olivine (Ol), Quarts (Qz) and Alunite (Al) were chosen. For the binary mixtures of An-Br, Br-Ol, Ol-An and Qz-Al, each time three mixtures were available with a 25%, 50% and 75% ratio by mass. These minerals have equivalent grain sizes (of the order of 100 $\mu$m) and densities (around 3 g/cm$^3$), making the volumetric and areal fractional abundances very close to these mass ratio's. The actual areal fractions are shown in the results section in Table VI. The main reason for selecting these four binary mixtures is that the fractional abundances are accurately estimated by the Hapke model.

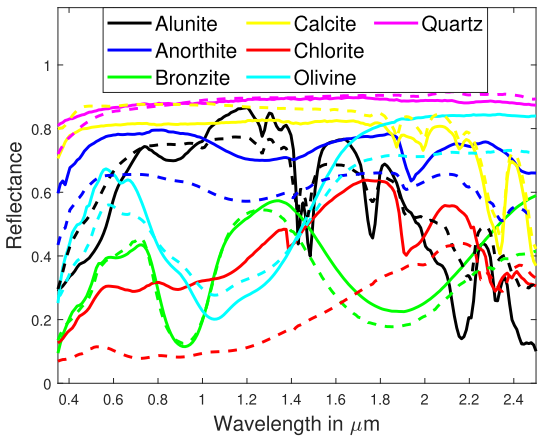


Fig. 5. Endmembers obtained from the USGS library (dashed) and the Relab data set (full line).

In order to validate the supervised approaches, a training data set is required. Moreover, we want to assess the ability of the proposed method to account for endmember variability. Therefore, we obtained endmembers for the five minerals from the USGS spectral library of minerals (https://speclab.cr.usgs.gov/spectral-lib.html). Endmembers from both USGS and Relab are shown in Fig. 5. It can be observed that the endmember spectra are quite different, since these endmembers were independently acquired by different sensors, and the used samples may exhibit some intrinsic variability as well. For the four binary mixtures, uniformly distributed groundtruth fractional abundances were generated (100 in total). Then, nonlinear spectra were artificially generated by applying the Hapke model on the USGS endmembers.

Finally, the mineral mixtures Calcite-Chlorite (Cal-Chl) were obtained both from the USGS library and the Relab data set. The Relab data set contains three mixtures of Calcite and Chlorite (25 %, 50%, and 75% by mass, respectively) while the USGS library data set contains two mixtures (33% and 66% by mass).

## V. Experiments and Results

The proposed method GSU was validated and compared to four unsupervised models, unsupervised GU and two other supervised approaches:

1) *LMM:* The linear unmixing model.
2) *Fan:* A bilinear mixture model.
3) *Hapke:* The Hapke model.
4) *NBRU [44]:* A neighbor-band ratio nonlinear unmixing approach which is robust against endmember variability
5) *GU:* Unsupervised GU. This is the first step of the proposed approach only.
6) *Softmax* (*SM*): An SM feedforward NN. It is a supervised approach that uses a training set to learn a

direct mapping of the observed spectra to the actual fractional abundances. In this network, the input layer contains $d$ nodes, representing the spectral bands of the actual spectra. There is one hidden layer consisting of $h = 5$ nodes and the output layer consisting of $p$ nodes, containing the true fractional abundances. The hyperbolic tangent function ($\tanh(a) = ((\exp(a) - \exp(-a))/(\exp(a) + \exp(-a)))$) is used as an activation function for the hidden layer and the SM activation ($f(a_j) = (\exp(a_j)/(\sum_{j=1}^{p} \exp(a_j)))$) for the output layer. This activation function guarantees the positivity and sum-to-one constraints on the abundances.

7) *GP_LMM:* This supervised method learns a mapping from the observed spectra to the linear model [22]. As the mapping procedure, Gaussian Processes is applied. In contrast to the proposed method, GP_LMM does not account for spectral variability and will not properly work in cross-sensor situations. Some endmember variability can however be taken into account by applying the learned mapping to map the endmember spectra of the test data set to the endmember spectra of the training data set, a procedure that cannot be performed with the direct mapping method SM.

A phenomenon that was observed in most of the applied data was a random scaling of the spectra due to variations in the acquisition conditions. For example, since the height of the sample holder was not easily controllable in the spectrometer, all the self-crafted mineral mixtures were randomly scaled with respect to each other. This phenomenon obviously affects the unmixing models, but also leads to ordering problems in the GU approach and to mapping errors in the supervised approaches. A normalization of all spectra by their length (i.e., a projection onto the unit circle), prior to the application of an unmixing procedure would solve this issue.

It is important to note that this projection is nonlinear and thus changes the nonlinearity of the manifolds. None of the mixing models are invariant to this transformation, hence we will not apply it prior to the model-based unmixing. The transformation will also introduce errors in the GU approach. In the supervised approaches however, it does not introduce extra errors, since the nonlinearity is changed both in the training and the test manifolds in a similar way. For this reason, we will normalize the spectra in all experiments prior to applying the methods GU, SM, GP_LMM, and the proposed method GSU.

All quantitative comparisons are provided by the abundance root mean squared error (RMSE), i.e., the error between the estimated fractional abundances ($\hat{\mathbf{A}}$) and the ground truth fractional abundances ($\mathbf{A}$)

$$\text{Abundance RMSE} = \sqrt{\frac{1}{pn}\sum_{k=1}^{p}\sum_{i=1}^{n}(\hat{\mathbf{A}}_{ki} - \mathbf{A}_{ki})^2} \times 100 \tag{17}$$

where $p$ and $n$ denote the number of endmembers and the number of mixed spectra, respectively.

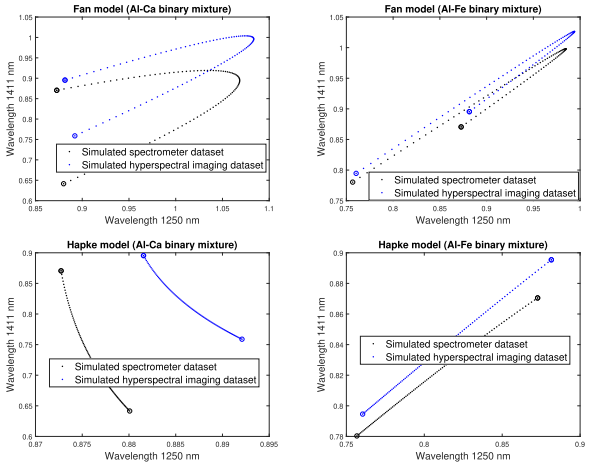


Fig. 6. Manifolds of the simulated spectrometer data set (black dots) and the simulated hyperspectral camera data set (blue dots), generated by the Fan model and the Hapke model.

### A. Experiments on Self-Crafted Mineral Data Set

*1) Experiment* 1 *(Simulated Manifolds):* In the first experiment, we generated simulated manifolds using the measured mineral endmembers from the camera and the spectrometer. From the mineral endmembers obtained from the AgriSpec spectrometer, groundtruth fractional abundances were generated uniformly from the unit simplex. Then, nonlinear spectra were artificially generated by applying the Fan and the Hapke model, respectively. In this way, ten binary mixtures: (Al-Ca), (Al-Fe), (Al-Si), (Al-Ti), (Ca-Fe), (Ca-Si), (Ca-Ti), (Fe-Si), (Fe-Ti) and (Si-Ti) were produced for each of both mixing models. Similarly, simulated manifolds were produced from the mineral endmembers obtained from the camera. Some of the data manifolds from both the spectrometer and camera are shown in Fig. 6. As can be observed from the figure, the manifolds simulated by the Fan and Hapke models are quite different, and applying one model on the manifold generated by the other model will not work. Also, the application of the linear model is expected to lead to large errors, in particular for the Fan manifolds. In the Al–Fe mixture, half of the manifold will be projected onto the second endmember. Another observation is that the manifolds of the camera and the spectrometer are obviously different, since also the endmembers are different (see Fig. 4).

In Table II, the abundance RMSEs of the simulated camera data are shown. Obviously, the Fan model results are not shown on the simulated Fan data and the Hapke model results are not shown on the simulated Hapke data. The supervised algorithms were trained on the simulated spectrometer data set. The geodesic distance was calculated by using all samples on the manifold. The outcomes of the experiments can be summarized as follows:

1) As expected, the performance of the unsupervised models is poor, since the manifolds of the simulated Hapke and Fan data are completely different. As an exception, the linear model performs quite well on the Hapke data set, because the manifolds are close to linear. NBRU

TABLE II

ABUNDANCE RMSE IN %. SUPERVISED ALGORITHMS WERE TRAINED ON THE SIMULATED SPECTROMETER DATA AND TESTED ON THE SIMULATED HYPERSPECTRAL CAMERA DATA

| Binary Mixture | Fan LMM | Fan Hapke | Fan NBRU | Fan GU | Fan SM | Fan GP_LMM | Fan GSU | Hapke LMM | Hapke Fan | Hapke NBRU | Hapke GU | Hapke SM | Hapke GP_LMM | Hapke GSU |
|---|---|---|---|---|---|---|---|---|---|---|---|---|---|---|
| Al-Ca | 47.59 | 48.26 | 5.11 | 8.92 | 29.16 | 0.83 | **0.65** | 9.08 | 57.28 | 11.06 | 9.07 | 29.16 | 1.98 | **1.38** |
| Al-Fe | 48.38 | 49.13 | 3.23 | 11.90 | 29.16 | 4.75 | **0.46** | 8.81 | 50.27 | 14.85 | 8.80 | 21.80 | 0.20 | **0.13** |
| Al-Si | 55.75 | 55.72 | 5.73 | 9.20 | 29.16 | 3.63 | **1.06** | 2.32 | 56.26 | 5.33 | 2.32 | 53.37 | 0.13 | **0.12** |
| Al-Ti | 54.64 | 54.80 | 3.26 | 9.38 | 19.73 | 2.57 | **0.08** | 3.74 | 55.35 | 5.69 | 3.73 | 29.13 | 0.15 | **0.03** |
| Ca-Fe | 47.88 | 48.47 | 6.24 | 11.34 | 29.16 | 4.59 | **1.13** | 9.22 | 50.65 | 1.12 | 9.21 | 29.16 | 0.44 | **0.40** |
| Ca-Si | 50.79 | 26.69 | 5.47 | 8.95 | 29.16 | 5.29 | **0.40** | 2.88 | 56.79 | 8.27 | 2.79 | 57.08 | **0.44** | 0.46 |
| Ca-Ti | 52.97 | 38.52 | 5.61 | 9.12 | 29.16 | 3.26 | **0.59** | **0.43** | 55.86 | 6.51 | 0.59 | 29.16 | 7.20 | 1.63 |
| Fe-Si | 49.97 | 50.25 | 4.26 | 11.08 | 28.61 | 4.11 | **1.48** | 6.75 | 51.39 | 11.74 | 6.75 | 29.49 | 0.15 | **0.05** |
| Fe-Ti | 50.22 | 50.44 | 2.85 | 10.49 | 20.79 | 4.90 | **0.57** | 6.80 | 52.12 | 12.61 | 6.79 | 29.16 | 0.85 | **0.41** |
| Si-Ti | 55.32 | 40.09 | 2.66 | 9.09 | 29.16 | 1.19 | **0.98** | 2.26 | 56.89 | 1.44 | 2.26 | 53.58 | 1.17 | **0.07** |

TABLE III

ESTIMATED FRACTIONAL ABUNDANCES ON THE SINGLE SENSOR EXPERIMENT (CAMERA DATA)

| Mixtures | Ground truth (first mineral) | LMM | Fan | Hapke | NBRU | GU | SM | GP_LMM | GSU |
|---|---|---|---|---|---|---|---|---|---|
| Al-Si | 0.593 | 0.437 | 0.012 | 0.473 | 0.300 | 0.290 | 0.503 | **0.543** | 0.496 |
| | 0.813 | 0.771 | 0.030 | **0.789** | 0.500 | 0.658 | 0.503 | 0.786 | 0.866 |
| | 0.929 | 0.918 | 0.036 | **0.926** | 0.864 | 0.837 | 0.503 | 0.890 | 0.959 |
| Ca-Si | 0.691 | 0.756 | 0.020 | 0.686 | 0.748 | 0.504 | 0.672 | 0.621 | **0.695** |
| | 0.871 | 0.837 | 0.027 | 0.803 | 1.000 | 0.822 | 0.907 | **0.882** | 0.921 |
| | 0.953 | 0.928 | 0.028 | 0.933 | 1.000 | 0.915 | **0.943** | 1.000 | 0.987 |
| Ca-Ti | 0.067 | 0.427 | 0.011 | 0.403 | 0.490 | 0.448 | **0.072** | 0.001 | 0.088 |
| | 0.177 | 0.667 | 0.021 | 0.626 | 0.834 | 0.759 | 0.173 | **0.180** | 0.226 |
| | 0.369 | 0.829 | 0.025 | 0.808 | 1.000 | 0.943 | 0.272 | **0.406** | 0.506 |
| Fe-Al | 0.525 | 0.485 | 0.917 | 0.356 | 0.695 | 0.712 | 0.446 | 0.536 | **0.527** |
| | 0.768 | 0.730 | 0.960 | 0.613 | 0.860 | 0.860 | 0.810 | **0.785** | 0.820 |
| | 0.901 | 0.886 | 0.984 | 0.824 | 0.894 | 0.906 | 0.910 | **0.896** | 0.944 |
| Fe-Ca | 0.418 | 0.515 | 0.916 | **0.361** | 0.518 | 0.611 | 0.485 | 0.501 | 0.483 |
| | 0.682 | 0.654 | 0.944 | 0.511 | 0.622 | 0.725 | 0.733 | 0.700 | **0.668** |
| | 0.865 | **0.858** | 0.978 | 0.779 | 0.828 | 0.887 | 0.838 | 0.887 | 0.889 |
| Fe-Si | 0.828 | 0.731 | 0.963 | 0.638 | 0.761 | 0.604 | 0.859 | **0.821** | 0.830 |
| | 0.935 | **0.932** | 0.999 | 0.910 | 0.977 | 0.951 | 0.921 | 0.942 | 0.994 |
| | 0.978 | 0.966 | 1.000 | 0.955 | 0.961 | 0.853 | **0.978** | 0.965 | 0.976 |
| Si-Ti | 0.011 | 0.082 | 0 | 0.088 | 0.083 | 0.320 | **0.016** | 0.019 | 0.004 |
| | 0.031 | 0.188 | 0 | 0.196 | 0.329 | 0.386 | **0.044** | 0.048 | 0.047 |
| | 0.087 | 0.554 | 0.007 | 0.572 | 0.618 | 0.502 | 0.113 | **0.108** | 0.124 |

performs equally well on the Hapke data set, and much better than the other models on the Fan data set.

2) The geodesic distance estimation of the abundances leads to errors of about 10% on the Fan data. On the Hapke data, it performs as well as the linear model, since the manifolds are close to linear. The errors are caused by the fact that the manifolds have a nonconstant curvature.
3) From the supervised approaches, the performance of SM is poor for any of the mixtures. This demonstrates that a direct mapping from the observed spectra to abundances will not work in a cross-sensor situation.
4) The results of GP_LMM are much better, since this method also maps the endmembers. Results however are clearly better for the Hapke data and vary a lot between mixtures.
5) Overall, the proposed approach GSU produces less than 2% abundance RMSE for most of the simulated binary mixtures. The proposed method is found to be very robust to endmember variability in the cross-sensor situation.

*2) Experiment* 2 *(Single Sensor Unmixing):* In the second experiment, we investigated the performance of the supervised methods when trained and tested on the data from the same sensor. For this, the real mixtures were applied. Four of the seven mixtures (with 1.25, 3.75, 6.25, and 8.75 g of the first mineral, respectively) were applied for training and the other three (2.5, 5.0, and 7.5 g) for testing. Results are shown in Table III for the camera data and Table IV for the spectrometer data. For comparison, the results of the unsupervised approaches are shown as well.

The outcomes of the experiments can be summarized as follows:

1) The Fan model always fails and observes a pure mineral rather than a mixture.
2) The Hapke and NBRU models do not perform better than the linear model. Both models, as well as GU generally perform poor on mixtures of minerals with large differences in grain size and/or density (e.g., Si-Ti).
3) Overall, all three supervised methods outperform the unsupervised approaches and were able to accurately predict fractional abundances from almost all binary mixtures. The algorithms perform equally well for the spectrometer and the hyperspectral camera data.
4) GP_LMM performs the best. The proposed method GSU is only slightly worse. In this single sensor experiment,

TABLE IV
ESTIMATED FRACTIONAL ABUNDANCES ON THE SINGLE SENSOR EXPERIMENT (SPECTROMETER DATA)

| Mixtures | Ground truth (first mineral) | LMM | Fan | Hapke | NBRU | GU | SM | GP_LMM | GSU |
|---|---|---|---|---|---|---|---|---|---|
| Al-Si | 0.593 | **0.571** | 0.002 | 0.606 | 0.634 | 0.329 | 0.448 | 0.508 | 0.554 |
| | 0.813 | 0.965 | 0.023 | 0.970 | 0.685 | 0.635 | 0.702 | 0.768 | **0.853** |
| | 0.929 | 1.000 | 0.022 | 1.000 | 0.700 | 0.833 | 0.946 | **0.927** | 0.978 |
| Ca-Si | 0.691 | 0.662 | 0 | 0.451 | **0.707** | 0.511 | 0.662 | 0.628 | 0.622 |
| | 0.871 | 0.850 | 0.002 | 0.820 | 0.899 | 0.829 | 0.799 | 0.903 | **0.891** |
| | 0.953 | 0.951 | 0.006 | 0.936 | 0.976 | 0.919 | 0.958 | **0.952** | 0.958 |
| Ca-Ti | 0.067 | 0.437 | 0.011 | 0.288 | 0.418 | 0.389 | 0.053 | 0.085 | **0.084** |
| | 0.177 | 0.670 | 0.009 | 0.581 | 0.705 | 0.671 | 0.258 | **0.174** | 0.222 |
| | 0.369 | 0.876 | 0.019 | 0.766 | 0.853 | 0.835 | 0.392 | **0.351** | 0.580 |
| Fe-Al | 0.525 | 0.436 | 0.921 | 0.349 | 0.678 | 0.732 | 0.472 | **0.535** | 0.612 |
| | 0.768 | 0.671 | 0.954 | 0.595 | 0.827 | 0.888 | 0.494 | **0.768** | 0.833 |
| | 0.901 | 0.953 | 0.993 | 0.938 | 0.886 | 0.941 | 0.494 | 0.883 | **0.901** |
| Fe-Ca | 0.418 | **0.427** | 0.921 | 0.381 | 0.574 | 0.654 | 0.490 | 0.547 | 0.488 |
| | 0.682 | 0.627 | 0.950 | 0.564 | 0.669 | 0.755 | 0.665 | 0.690 | **0.675** |
| | 0.865 | 0.927 | 0.991 | 0.903 | **0.853** | 0.899 | 0.911 | 0.890 | 0.893 |
| Fe-Si | 0.828 | 0.707 | 0.972 | 0.662 | 0.728 | 0.681 | 0.844 | **0.833** | 0.820 |
| | 0.935 | 0.996 | 0.999 | 0.998 | 0.899 | 0.960 | 0.882 | **0.929** | 0.977 |
| | 0.978 | 1.000 | 1.000 | 1.000 | 0.917 | 0.877 | 0.966 | **0.974** | 0.958 |
| Si-Ti | 0.011 | 0.178 | 0 | 0.151 | 0.273 | 0.370 | **0.012** | 0.016 | 0.001 |
| | 0.031 | 0.225 | 0 | 0.219 | 0.411 | 0.404 | 0.021 | **0.028** | 0.010 |
| | 0.087 | 0.394 | 0.003 | 0.418 | 0.508 | 0.483 | 0.041 | **0.075** | 0.055 |

the use of the geodesic abundance estimation step has no extra advantage.

5) Remark that the fractional abundances, estimated by GU on the camera data and the spectrometer data are very similar, because the underlying nonlinearity is the same. This further validates our claim that GU is invariant to external spectral variability.

*3) Experiment* 3 *(Cross Sensor Unmixing):* In the third experiment, we investigated the performance of the supervised approaches in a cross sensor situation. For this, we trained the algorithms on the spectrometer data and applied the learned models on the camera data. Similarly, we trained the algorithms on the camera data and applied the learned models on the spectrometer data. We do not show the results of the unsupervised approaches, since they have been treated in the previous experiment.

Results are shown in Table V. The results clearly show the advantage of the proposed strategy to tackle the endmember variability. GSU outperforms the other methods in almost all cases. SM performs the worst, while GP_LMM that takes endmember variability partially into account, performs reasonably well on some mixtures but poor on others.

### B. Experiments on RELAB Data Set

*1) Experiment* 4 *(Cross Sensor Experiment on Simulated USGS and Real Relab Mineral Mixtures):* From Fig. 5, we can observe that there is a large variability between the endmembers obtained from the USGS spectral library and the Relab data set. The applied minerals have similar densities and grain sizes, well above the SWIR wavelength ranges, so that the Hapke model is expected to be efficient.

In the fourth experiment, we investigated the performance of the supervised approaches for predicting fractional abundances of Relab mineral mixtures when the algorithms were trained on simulated mineral mixtures by the Hapke model on the USGS endmembers. For comparison, the results of the unsupervised approaches are shown as well.

In Table VI, we show the results. The Hapke model performs the best. All other unsupervised approaches perform poor. The Fan model fails. Except for the binary mixture of Olivine and Bronzite, NBRU did not perform well. The GU approach and LMM produce similar results. From the supervised approaches, SM fails and GP_LMM performs poor on two of the four mixtures. Overall, GSU was able to predict fractional abundances of the Relab data set accurately, sometimes even better than the Hapke model. This demonstrates the robustness of the proposed methodology with respect to endmember variability.

*2) Experiment* 5 *(Cross Sensor Experiment on Real USGS and Relab Mineral Data):* In the final experiment, we investigated the performance of the supervised approaches on Cal-Chl mixtures when trained on Relab spectra and tested on USGS spectra. Similarly, the algorithms were trained on USGS spectra and tested on Relab spectra. For comparison, the result of the unsupervised methods is shown as well.

Results are shown in Table VII. Except for the proposed approach, all methods including the Hapke model perform poor.

### C. Experiment 6: Ternary Mixtures

The proposed method and the conducted experiments all are focused on the application on binary mixtures. In principle, the entire procedure is applicable to mixtures of higher number of materials. The only step that is highly influenced is the geodesic abundance estimation, which now requires the estimation of geodesic distances on nonlinear simplices of higher dimensionality using the Dijkstra algorithm which is expected to enlarge the complexity and to introduce the estimation errors, unless a large number of datapoints is available. The application of the methodology on mixtures

TABLE V
CROSS SENSOR RESULTS ON SELF-CRAFTED MINERAL MIXTURES

| Mixtures | Ground truth (first mineral) | HSI SM | HSI GP_LMM | HSI GSU | Spectrometer SM | Spectrometer GP_LMM | Spectrometer GSU |
|---|---|---|---|---|---|---|---|
| Al-Si | 0.385 | 0.999 | 0.194 | **0.354** | 0.969 | 0.745 | **0.488** |
| | 0.593 | 0.956 | 0.266 | **0.536** | 0.973 | 0.885 | **0.638** |
| | 0.724 | 0.998 | 0.439 | **0.872** | 0.974 | 0.976 | **0.846** |
| | 0.813 | 0.992 | 0.538 | **0.655** | 0.974 | 0.979 | **0.856** |
| | 0.879 | 0.999 | 0.607 | **0.803** | 0.974 | 0.981 | **0.880** |
| | 0.929 | 0.992 | 0.664 | **0.700** | 0.974 | 0.966 | **0.916** |
| | 0.968 | 0.998 | 0.755 | **0.967** | 0.974 | 0.941 | **0.969** |
| Ca-Si | 0.494 | 0.394 | 0.521 | **0.440** | 0.319 | 0.422 | **0.513** |
| | 0.691 | 0.559 | 0.606 | **0.656** | 0.482 | 0.511 | **0.725** |
| | 0.802 | 0.675 | 0.660 | **0.728** | 0.790 | 0.633 | **0.820** |
| | 0.871 | 0.733 | **0.882** | 0.860 | 0.861 | 0.795 | **0.894** |
| | 0.919 | 0.822 | **0.918** | 0.901 | 0.896 | 0.812 | **0.934** |
| | 0.953 | 0.795 | 0.926 | **0.931** | 0.892 | 0.852 | **0.966** |
| | 0.979 | 0.877 | 0.940 | **0.933** | 0.887 | 0.849 | **0.990** |
| Ca-Ti | 0.030 | 0.061 | 0.005 | **0.031** | 0.018 | 0.025 | **0.030** |
| | 0.067 | 0.085 | 0.011 | **0.084** | 0.010 | 0.100 | **0.053** |
| | 0.115 | 0.084 | 0.020 | **0.123** | 0.020 | 0.166 | **0.100** |
| | 0.177 | 0.232 | 0.065 | **0.194** | 0.024 | 0.324 | **0.170** |
| | 0.265 | 0.170 | 0.093 | **0.297** | 0.047 | 0.400 | **0.249** |
| | 0.369 | 0.291 | 0.123 | **0.464** | 0.098 | 0.448 | **0.315** |
| | 0.599 | 0.278 | 0.130 | **0.604** | 0.200 | 0.463 | **0.607** |
| Fe-Al | 0.321 | 0.589 | 0.305 | **0.318** | 0.934 | 0.329 | **0.318** |
| | 0.525 | 0.666 | 0.486 | **0.537** | 0.390 | 0.546 | **0.520** |
| | 0.666 | 0.606 | **0.655** | 0.683 | 0.174 | 0.745 | **0.647** |
| | 0.768 | 0.647 | 0.729 | **0.757** | 0.433 | 0.857 | **0.790** |
| | 0.847 | 0.601 | **0.799** | 0.940 | 0.483 | 0.976 | **0.884** |
| | 0.901 | 0.605 | 0.807 | **0.834** | 0.725 | 0.974 | **0.890** |
| | 0.958 | 0.540 | 0.825 | **0.862** | 0.817 | **0.999** | 0.837 |
| Fe-Ca | 0.236 | 0.096 | 0.641 | **0.235** | 0.053 | 0.017 | **0.237** |
| | 0.418 | 0.297 | 0.763 | **0.433** | 0.105 | 0.269 | **0.413** |
| | 0.563 | 0.397 | 0.783 | **0.570** | 0.214 | 0.323 | **0.547** |
| | 0.682 | 0.619 | 0.840 | **0.687** | 0.481 | 0.504 | **0.675** |
| | 0.781 | 0.790 | 0.890 | **0.792** | 0.771 | 0.696 | **0.769** |
| | 0.865 | 0.808 | 0.921 | **0.867** | 0.760 | 0.838 | **0.863** |
| | 0.937 | 0.738 | 0.935 | **0.936** | 0.901 | 0.913 | **0.936** |
| Fe-Si | 0.674 | 0.226 | 0.613 | **0.673** | 0.483 | 0.735 | **0.679** |
| | 0.828 | 0.302 | 0.784 | **0.806** | 0.633 | 0.881 | **0.837** |
| | 0.897 | 0.215 | 0.879 | **0.893** | 0.714 | 0.936 | **0.920** |
| | 0.935 | 0.506 | 0.957 | **0.938** | 0.731 | 0.972 | **0.938** |
| | 0.960 | 0.469 | 0.946 | **0.962** | 0.798 | 0.973 | **0.951** |
| | 0.978 | 0.443 | 0.939 | **0.967** | 0.782 | **0.972** | 0.963 |
| | 0.990 | 0.240 | 0.918 | **0.939** | 0.873 | **0.962** | 0.955 |
| Si-Ti | 0.005 | 0.074 | 0.042 | **0.004** | 0.050 | 0.057 | **0.005** |
| | 0.011 | 0.046 | 0.066 | **0.008** | 0.045 | 0.024 | **0.020** |
| | 0.018 | 0.087 | 0.053 | **0.006** | 0.022 | **0.021** | 0.022 |
| | 0.031 | 0.184 | 0.143 | **0.030** | 0.009 | 0.012 | **0.036** |
| | 0.051 | 0.230 | 0.108 | **0.042** | 0.008 | 0.009 | **0.059** |
| | 0.087 | 0.210 | 0.265 | **0.105** | 0.008 | 0.020 | **0.083** |
| | 0.182 | 0.227 | 0.289 | **0.181** | 0.005 | 0.053 | **0.187** |

TABLE VI
CROSS SENSOR RESULTS ON REAL RELAB MINERAL MIXTURES, WHERE SUPERVISED APPROACHES ARE TRAINED ON SIMULATED USGS MIXTURES

| Minerals | Ground truth (first mineral) | LMM | Fan | Hapke | NBRU | GU | SM | GP_LMM | GSU |
|---|---|---|---|---|---|---|---|---|---|
| Br-An | 0.217 | 0.497 | 0.628 | 0.203 | 0.381 | 0.496 | 0.278 | **0.222** | 0.236 |
| | 0.454 | 0.739 | 0.823 | **0.461** | 0.610 | 0.737 | 0.040 | 0.424 | 0.492 |
| | 0.714 | 0.892 | 0.930 | **0.732** | 0.801 | 0.891 | 0.052 | 0.606 | 0.743 |
| Ol-Br | 0.248 | 0.118 | 0.068 | **0.236** | 0.212 | 0.131 | 0.971 | 0.416 | 0.265 |
| | 0.498 | 0.269 | 0.172 | **0.502** | 0.430 | 0.281 | 0.986 | 0.677 | 0.523 |
| | 0.748 | 0.500 | 0.369 | 0.772 | 0.685 | 0.505 | 0.991 | 0.931 | **0.771** |
| An-Ol | 0.288 | 0.163 | 0.034 | **0.315** | 0.221 | 0.175 | 0.0 | 0.184 | 0.235 |
| | 0.548 | 0.348 | 0.108 | **0.588** | 0.429 | 0.357 | 0.0 | 0.505 | 0.464 |
| | 0.784 | 0.575 | 0.261 | 0.811 | 0.662 | 0.579 | 0.0 | **0.798** | 0.699 |
| Al-Qz | 0.240 | 0.660 | 0.829 | 0.305 | 0.488 | 0.638 | 0.073 | 0.408 | **0.300** |
| | 0.486 | 0.794 | 0.890 | **0.488** | 0.685 | 0.772 | 0.025 | 0.670 | 0.544 |
| | 0.740 | 0.925 | 0.967 | 0.785 | 0.837 | 0.923 | 0.990 | 0.999 | **0.765** |

of higher number of materials is somewhat out of the scope of this work, and we regard this as future work. However, as an illustration, we include a small experiment on ternary mixtures. For this, we generated simulated manifolds using the measured mineral endmembers Al, Ca, and Fe from the camera and the spectrometer. Groundtruth fractional abundances were

TABLE VII
CROSS SENSOR RESULTS ON REAL RELAB MINERAL MIXTURES, WHERE SUPERVISED APPROACHES ARE TRAINED ON REAL USGS MIXTURES AND VICE-VERSA

| Minerals | Ground truth (first mineral) | LMM | Fan | Hapke | NBRU | GU | SM | GP_LMM | GSU |
|---|---|---|---|---|---|---|---|---|---|
| Chl-Cal (USGS) | 0.34 | 0.853 | 0.876 | 0.518 | 0.706 | 0.731 | 0.50 | 0.750 | **0.328** |
| | 0.67 | 0.970 | 0.976 | 0.863 | 0.885 | 0.902 | 0.50 | 0.834 | **0.685** |
| Chl-Cal (Relab) | 0.258 | 0.718 | 0.819 | 0.491 | 0.480 | 0.710 | 0.492 | 0.897 | **0.334** |
| | 0.510 | 0.849 | 0.905 | 0.696 | 0.647 | 0.834 | 0.496 | 0.947 | **0.520** |
| | 0.758 | 0.973 | 0.982 | 0.986 | 0.861 | 0.945 | 0.497 | 0.931 | **0.817** |

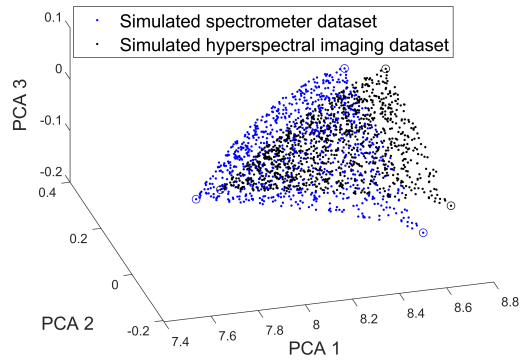


Fig. 7. Manifolds of the simulated spectrometer data set (black dots) and the simulated hyperspectral camera data set (blue dots), generated by the Hapke model.

generated uniformly from the unit simplex. Then, nonlinear spectra were artificially generated by applying the Hapke model. In this way, ternary mixtures of (Al–Ca–Fe) were produced. principal component analysis (PCA) reduced data manifolds from both the spectrometer and camera are shown in Fig. 7. As can be observed, the manifolds of the camera and the spectrometer are obviously different, since also the endmembers are different (see Fig. 4).

Then, the supervised algorithms were trained on the spectrometer manifold and tested on the camera manifold. The geodesic distance was calculated by using all samples on the manifold. While none of the unmixing models was able to estimate the abundances accurately, the proposed approach GSU produced an abundance RMSE of 3.6%, while the error of GP_LMM was only 0.31%. Although the error is acceptable, most of it can be attributed to errors in estimating the geodesic paths during the geodesic abundance estimation step.

## VI. DISCUSSION

From the experiments, the following general conclusions can be drawn:

1) In general, the LMM does not perform well on intimate mixtures of mineral powders. The good performance of the LMM for some binary mixture of the self-crafted data set suggests that the nonlinearity in those data sets is not very complex. This might be due to the fact that some minerals in the mixtures have similar spectral behavior.
2) The Fan model is not suitable for estimating fractional abundances of binary mixtures of mineral powders.
3) In general, the Hapke model estimates the fractional abundances of the intimate mixtures reasonably well. As an exception, the Hapke model produced large errors on the binary mixtures of Calcite and Chlorite, Calcium and Titanium, and Silica and Titanium.
4) GU generally produces poor estimations. This is because the data manifold comprises a nonlinear relationship between the arc length and the fractional abundances. When manifolds contain the same underlying nonlinearity, GU produces the same abundance estimations, demonstrating that the geodesic abundance estimation is invariant to external spectral variability.
5) Most of the supervised methods can estimate fractional abundances of test spectra accurately when trained on the same data manifold.
6) In cross sensor situations, SM performs poor, since it cannot cope with endmember variability. In GP_LMM, the endmember variability is partially taken into account, by mapping the endmembers along with the mixtures, leading to improved results.
7) The proposed approach GSU was found to be the most consistent and performed well for almost all mineral mixtures used in this study. This demonstrates the potential of the proposed methodology, in particular, in cross sensor situations.

All methods were developed in MATLAB and ran on an Intel Core $i7$-$8700K$ CPU, 3.20 GHz machine with six cores. The computational cost of the geodesic abundance estimation is 1–2 orders of magnitude lower than that of the supervised approaches, even in the case of the ternary mixtures. The runtime of GU exponentially grows with the number of datapoints, but was well below 1 s in all experiment. The runtime of SM was of the order of 1 s, while it was of the order of 10 s for the other supervised approaches on each sample.

## VII. CONCLUSION

In this work, we have proposed a strategy for nonlinear unmixing, taking into account spectral variability. The method contains a GU step that is invariant to endmember variability, and a supervised mapping step to learn the nonlinearity. The approach was validated and compared to a number of spectral mixing models and supervised unmixing approaches on binary mixtures of mineral powders, in single sensor and cross sensor situations. In future work, we will adapt the proposed method to be applicable on polynary mixtures.

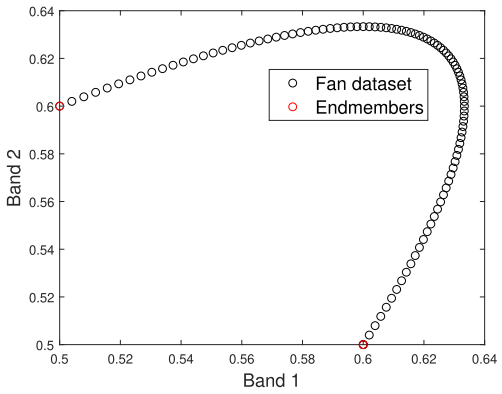


Fig. 8. Data manifold of the Fan model.

## APPENDIX

A nonlinear relationship exists between the arc length and the fractional abundances in data manifolds that are generated by nonlinear mixing models. As a result, the geodesic distance between a mixture and an endmember does not provide the correct fractional abundance.

As an illustration, let us look at the Fan model in two dimensions. Consider a path in the spectral space from endmember $\mathbf{e}_1 = \begin{bmatrix}0.6\\0.5\end{bmatrix}$ to endmember $\mathbf{e}_2 = \begin{bmatrix}0.5\\0.6\end{bmatrix}$, parametrized by the fractional abundance of endmember $\mathbf{e}_2$ ($t \in [0, 1]$). Then, according to the Fan model, each data point of the manifold can be described by the following equation:

$$\mathbf{y} = \begin{bmatrix}0.6\\0.5\end{bmatrix}(1-t) + \begin{bmatrix}0.5\\0.6\end{bmatrix}t + \begin{bmatrix}0.6\\0.5\end{bmatrix} \odot \begin{bmatrix}0.5\\0.6\end{bmatrix}(1-t)t \quad (18)$$

The arc length (geodesic distance) between $\mathbf{e}_1$ and the datapoint $\mathbf{y} = \begin{bmatrix}y_1\\y_2\end{bmatrix}$ (see Fig. 8 for the data manifold) can be determined as follows:

$$\begin{aligned}\text{Arc length}(t) &= \int_0^t \sqrt{\left(\frac{\mathrm{d}y_1}{\mathrm{d}t}\right)^2 + \left(\frac{\mathrm{d}y_2}{\mathrm{d}t}\right)^2}\,\mathrm{d}t \\ &= \int_0^t \sqrt{(0.2-0.6t)^2 + (0.4-0.6t)^2}\mathrm{d}t \\ &= 0.1(t-0.5)\sqrt{18t^2-18t+5} - 0.0117851 \\ &\quad \times \operatorname{arcsinh}(3-6t) + 0.1332340 \end{aligned} \quad (19)$$

which is clearly nonlinearly related to $t$. This nonlinear relationship is caused by the fact that the curvature($\kappa$) of the manifold is not constant

$$\begin{aligned}\kappa &= \frac{\left\|\frac{\mathrm{dy}}{\mathrm{d}t} \times \frac{\mathrm{d}^2\mathrm{y}}{\mathrm{d}t^2}\right\|}{\left\|\frac{\mathrm{dy}}{\mathrm{d}t}\right\|^3} \\ &= \frac{0.12}{((0.2-0.6t)^2 + (0.4-0.6t)^2)^{3/2}} \end{aligned} \quad (20)$$

where $\times$ denotes the cross product between two vectors and $\|.\|$ is the Euclidean norm of the vector.

## ACKNOWLEDGMENT

The authors would like to thank the company Engie-Laborelec for the use of their hyperspectral SWIR camera, and Prof. R. Samson for the use of the spectrometer.

## REFERENCES

[1] N. Keshava and J. F. Mustard, "Spectral unmixing," *IEEE Signal Process. Mag.*, vol. 19, no. 1, pp. 44–57, Jan. 2002.
[2] J. W. Boardman, "Geometric mixture analysis of imaging spectrometry data," in *Proc. IEEE Int. Geosci. Remote Sens. Symp. (IGARSS)*, vol. 4, Aug. 1994, pp. 2369–2371.
[3] D. C. Heinz and Chein-I-Chang, "Fully constrained least squares linear spectral mixture analysis method for material quantification in hyperspectral imagery," *IEEE Trans. Geosci. Remote Sens.*, vol. 39, no. 3, pp. 529–545, Mar. 2001.
[4] R. Heylen, M. Parente, and P. Gader, "A review of nonlinear hyperspectral unmixing methods," *IEEE J. Sel. Topics Appl. Earth Observ. Remote Sens.*, vol. 7, no. 6, pp. 1844–1868, Jun. 2014.
[5] W. Fan, B. Hu, J. Miller, and M. Li, "Comparative study between a new nonlinear model and common linear model for analysing laboratory simulated-forest hyperspectral data," *Int. J. Remote Sens.*, vol. 30, no. 11, pp. 2951–2962, Jun. 2009.
[6] R. Heylen and P. Scheunders, "A multilinear mixing model for nonlinear spectral unmixing," *IEEE Trans. Geosci. Remote Sens.*, vol. 54, no. 1, pp. 240–251, Jan. 2016.
[7] A. Marinoni and P. Gamba, "A novel approach for efficient $p$-linear hyperspectral unmixing," *IEEE J. Sel. Topics Signal Process.*, vol. 9, no. 6, pp. 1156–1168, Sep. 2015.
[8] A. Marinoni, J. Plaza, A. Plaza, and P. Gamba, "Nonlinear hyperspectral unmixing using nonlinearity order estimation and polytope decomposition," *IEEE J. Sel. Topics Appl. Earth Observ. Remote Sens.*, vol. 8, no. 6, pp. 2644–2654, Jun. 2015.
[9] A. Marinoni, A. Plaza, and P. Gamba, "Harmonic mixture modeling for efficient nonlinear hyperspectral unmixing," *IEEE J. Sel. Topics Appl. Earth Observ. Remote Sens.*, vol. 9, no. 9, pp. 4247–4256, Sep. 2016.
[10] B. Hapke, R. Nelson, and W. Smythe, "The opposition effect of the moon: Coherent backscatter and shadow hiding," *Icarus*, vol. 133, no. 1, pp. 89–97, 1998.
[11] B. Hapke, "Bidirectional reflectance spectroscopy: 1. Theory," *J. Geophys. Res., Solid Earth*, vol. 86, no. B4, pp. 3039–3054, Apr. 1981.
[12] J. Chen, C. Richard, and P. Honeine, "Nonlinear unmixing of hyperspectral data based on a linear-mixture/nonlinear-fluctuation model," *IEEE Trans. Signal Process.*, vol. 61, no. 2, pp. 480–492, Jan. 2013.
[13] Y. Gu, S. Wang, and X. Jia, "Spectral unmixing in multiple-kernel Hilbert space for hyperspectral imagery," *IEEE Trans. Geosci. Remote Sens.*, vol. 51, no. 7, pp. 3968–3981, Jul. 2013.
[14] J. Broadwater, R. Chellappa, A. Banerjee, and P. Burlina, "Kernel fully constrained least squares abundance estimates," in *Proc. IEEE Int. Geosci. Remote Sens. Symp.*, Jul. 2007, pp. 4041–4044.
[15] J. Broadwater and A. Banerjee, "A comparison of kernel functions for intimate mixture models," in *Proc. 1st Workshop Hyperspectral Image Signal Process., Evol. Remote Sens.*, Aug. 2009, pp. 1–4.
[16] G. Foody, "Relating the land-cover composition of mixed pixels to artificial neural network classification output," *Photogr. Eng. Remote Sens.*, vol. 62, no. 5, pp. 491–499, 1996.
[17] G. M. Foody, R. M. Lucas, P. J. Curran, and M. Honzak, "Non-linear mixture modelling without end-members using an artificial neural network," *Int. J. Remote Sens.*, vol. 18, no. 4, pp. 937–953, Mar. 1997.
[18] P. M. Atkinson, M. E. J. Cutler, and H. Lewis, "Mapping sub-pixel proportional land cover with AVHRR imagery," *Int. J. Remote Sens.*, vol. 18, no. 4, pp. 917–935, Mar. 1997.
[19] A. Okujeni, S. van der Linden, L. Tits, B. Somers, and P. Hostert, "Support vector regression and synthetically mixed training data for quantifying urban land cover," *Remote Sens. Environ.*, vol. 137, pp. 184–197, Oct. 2013.
[20] G. A. Licciardi and F. Del Frate, "Pixel unmixing in hyperspectral data by means of neural networks," *IEEE Trans. Geosci. Remote Sens.*, vol. 49, no. 11, pp. 4163–4172, Nov. 2011.
[21] B. Koirala, R. Heylen, and P. Scheunders, "A neural network method for nonlinear hyperspectral unmixing," in *Proc. IEEE Int. Geosci. Remote Sens. Symp. (IGARSS)*, Jul. 2018, pp. 4233–4236.
[22] B. Koirala, M. Khodadadzadeh, C. Contreras, Z. Zahiri, R. Gloaguen, and P. Scheunders, "A supervised method for nonlinear hyperspectral unmixing," *Remote Sens.*, vol. 11, no. 20, p. 2458, Oct. 2019.

[23] L. Drumetz, J. Chanussot, and C. Jutten, "Variability of the endmembers in spectral unmixing," in *Hyperspectral Imaging* (*Data Handling in Science and Technology*), vol. 32, J. M. Amigo, Ed. Amsterdam, The Netherlands: Elsevier, 2020, ch. 2.7, pp. 167–203.
[24] B. Somers, G. P. Asner, L. Tits, and P. Coppin, "Endmember variability in spectral mixture analysis: A review," *Remote Sens. Environ.*, vol. 115, no. 7, pp. 1603–1616, Jul. 2011.
[25] A. Zare and K. C. Ho, "Endmember variability in hyperspectral analysis: Addressing spectral variability during spectral unmixing," *IEEE Signal Process. Mag.*, vol. 31, no. 1, pp. 95–104, Jan. 2014.
[26] D. A. Roberts, M. Gardner, R. Church, S. Ustin, G. Scheer, and R. O. Green, "Mapping chaparral in the Santa Monica mountains using multiple endmember spectral mixture models," *Remote Sens. Environ.*, vol. 65, no. 3, pp. 267–279, Sep. 1998.
[27] B. Somers, M. Zortea, A. Plaza, and G. P. Asner, "Automated extraction of image-based endmember bundles for improved spectral unmixing," *IEEE J. Sel. Topics Appl. Earth Observ. Remote Sens.*, vol. 5, no. 2, pp. 396–408, Apr. 2012.
[28] T. Uezato, R. J. Murphy, A. Melkumyan, and A. Chlingaryan, "A novel endmember bundle extraction and clustering approach for capturing spectral variability within endmember classes," *IEEE Trans. Geosci. Remote Sens.*, vol. 54, no. 11, pp. 6712–6731, Nov. 2016.
[29] C. A. Bateson, G. P. Asner, and C. A. Wessman, "Endmember bundles: A new approach to incorporating endmember variability into spectral mixture analysis," *IEEE Trans. Geosci. Remote Sens.*, vol. 38, no. 2, pp. 1083–1094, Mar. 2000.
[30] T. Uezato, R. J. Murphy, A. Melkumyan, and A. Chlingaryan, "A novel spectral unmixing method incorporating spectral variability within endmember classes," *IEEE Trans. Geosci. Remote Sens.*, vol. 54, no. 5, pp. 2812–2831, May 2016.
[31] L. Drumetz, M.-A. Veganzones, S. Henrot, R. Phlypo, J. Chanussot, and C. Jutten, "Blind hyperspectral unmixing using an extended linear mixing model to address spectral variability," *IEEE Trans. Image Process.*, vol. 25, no. 8, pp. 3890–3905, Aug. 2016.
[32] P.-A. Thouvenin, N. Dobigeon, and J.-Y. Tourneret, "Hyperspectral unmixing with spectral variability using a perturbed linear mixing model," *IEEE Trans. Signal Process.*, vol. 64, no. 2, pp. 525–538, Jan. 2016.
[33] D. Hong, N. Yokoya, J. Chanussot, and X. X. Zhu, "An augmented linear mixing model to address spectral variability for hyperspectral unmixing," *IEEE Trans. Image Process.*, vol. 28, no. 4, pp. 1923–1938, Apr. 2019.
[34] A. Halimi, N. Dobigeon, and J.-Y. Tourneret, "Unsupervised unmixing of hyperspectral images accounting for endmember variability," *IEEE Trans. Image Process.*, vol. 24, no. 12, pp. 4904–4917, Dec. 2015.
[35] Y. Zhou, A. Rangarajan, and P. D. Gader, "A Gaussian mixture model representation of endmember variability in hyperspectral unmixing," *IEEE Trans. Image Process.*, vol. 27, no. 5, pp. 2242–2256, May 2018.
[36] Y. Zhou, E. B. Wetherley, and P. D. Gader, "Unmixing urban hyperspectral imagery using probability distributions to represent endmember variability," *Remote Sens. Environ.*, vol. 246, Sep. 2020, Art. no. 111857.
[37] T. Uezato, M. Fauvel, and N. Dobigeon, "Hyperspectral unmixing with spectral variability using adaptive bundles and double sparsity," *IEEE Trans. Geosci. Remote Sens.*, vol. 57, no. 6, pp. 3980–3992, Jun. 2019.
[38] D. Hong and X. X. Zhu, "SULoRA: Subspace unmixing with low-rank attribute embedding for hyperspectral data analysis," *IEEE J. Sel. Topics Signal Process.*, vol. 12, no. 6, pp. 1351–1363, Dec. 2018.
[39] L. Drumetz, J. Chanussot, C. Jutten, W.-K. Ma, and A. Iwasaki, "Spectral variability aware blind hyperspectral image unmixing based on convex geometry," *IEEE Trans. Image Process.*, vol. 29, pp. 4568–4582, 2020.
[40] L. Drumetz, B. Ehsandoust, J. Chanussot, B. Rivet, M. Babaie-Zadeh, and C. Jutten, "Relationships between nonlinear and space-variant linear models in hyperspectral image unmixing," *IEEE Signal Process. Lett.*, vol. 24, no. 10, pp. 1567–1571, Oct. 2017.
[41] A. Halimi, P. Honeine, and J. M. Bioucas-Dias, "Hyperspectral unmixing in presence of endmember variability, nonlinearity, or mismodeling effects," *IEEE Trans. Image Process.*, vol. 25, no. 10, pp. 4565–4579, Oct. 2016.
[42] A. Halimi, J. M. Bioucas-Dias, N. Dobigeon, G. S. Buller, and S. McLaughlin, "Fast hyperspectral unmixing in presence of nonlinearity or mismodeling effects," *IEEE Trans. Comput. Imag.*, vol. 3, no. 2, pp. 146–159, Jun. 2017.
[43] W. Luo, L. Gao, R. Zhang, A. Marinoni, and B. Zhang, "Bilinear normal mixing model for spectral unmixing," *IET Image Process.*, vol. 13, no. 2, pp. 344–354, Feb. 2019.
[44] K. Siebels, K. Goita, and M. Germain, "Estimation of mineral abundance from hyperspectral data using a new supervised neighbor-band ratio unmixing approach," *IEEE Trans. Geosci. Remote Sens.*, vol. 58, no. 10, pp. 6754–6766, Oct. 2020.
[45] Z. Wang, M. He, Z. Ye, K. Xu, Y. Nian, and B. Huang, "Reconstruction of hyperspectral images from spectral compressed sensing based on a multitype mixing model," *IEEE J. Sel. Topics Appl. Earth Observ. Remote Sens.*, vol. 13, pp. 2304–2320, 2020.
[46] R. Heylen, D. Burazerovic, and P. Scheunders, "Non-linear spectral unmixing by geodesic simplex volume maximization," *IEEE J. Sel. Topics Signal Process.*, vol. 5, no. 3, pp. 534–542, Jun. 2011.
[47] M. Zhao, J. Chen, and Z. He, "A laboratory-created dataset with ground truth for hyperspectral unmixing evaluation," *IEEE J. Sel. Topics Appl. Earth Observ. Remote Sens.*, vol. 12, no. 7, pp. 2170–2183, Jul. 2019.
[48] A. Halimi, Y. Altmann, N. Dobigeon, and J.-Y. Tourneret, "Nonlinear unmixing of hyperspectral images using a generalized bilinear model," *IEEE Trans. Geosci. Remote Sens.*, vol. 49, no. 11, pp. 4153–4162, Nov. 2011.
[49] Y. Altmann, A. Halimi, N. Dobigeon, and J.-Y. Tourneret, "Supervised nonlinear spectral unmixing using a postnonlinear mixing model for hyperspectral imagery," *IEEE Trans. Image Process.*, vol. 21, no. 6, pp. 3017–3025, Jun. 2012.
[50] J. F. Mustard and C. M. Pieters, "Quantitative abundance estimates from bidirectional reflectance measurements," *J. Geophys. Res., Solid Earth*, vol. 92, no. B4, pp. E617–E626, Mar. 1987.
[51] E. W. Dijkstra, "A note on two problems in connexion with graphs," *Numerische Math.*, vol. 1, no. 1, pp. 269–271, Dec. 1959.
[52] C. Rasmussen and C. Williams, *Gaussian Processes for Machine Learning*. New York, NY, USA: MIT Press, 2006.
[53] J. F. Mustard and C. M. Pieters, "Photometric phase functions of common geologic minerals and applications to quantitative analysis of mineral mixture reflectance spectra," *J. Geophys. Res., Solid Earth*, vol. 94, no. B10, pp. 13619–13634, Oct. 1989.

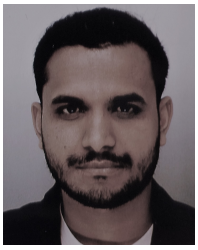

**Bikram Koirala** (Graduate Student Member, IEEE) received the B.S. degree in geomatic engineering from Purbanchal University, Biratnagar, Nepal, in 2011, and the M.S. degree in geomatic engineering from the University of Stuttgart, Stuttgart, Germany, in 2016.

In 2017, he joined Vision Laboratory, Department of Physics, University of Antwerp, Antwerp, Belgium, as a Ph.D. Researcher. His research interest includes machine learning and hyperspectral image (HSI) processing.

**Zohreh Zahiri** (Member, IEEE) received the bachelor's degree in civil engineering from Shahid Ashrafi Esfahani University, Isfahan, Iran, in 2009, the M.S. degree in architectural conservation from the Isfahan University of Art, Isfahan, in 2013, and the Ph.D. degree in characterization of facade materials using close-range hyperspectral data from the Department of Civil Engineering, University College Dublin (UCD), Dublin, Ireland, in 2018.

She is a Postdoctoral Researcher with Vision Laboratory, Department of Physics, University of Antwerp, Antwerp, Belgium. Her research interests are the application of hyperspectral imaging in civil engineering and related areas as well as data analysis methods.

**Alfredo Lamberti** received the M.S. degree in aerospace engineering and astronautics from the University of Naples Federico II, Naples, Italy, in 2011, and the Ph.D. degree in engineering sciences from Vrije Universiteit Brussel, Brussels, Belgium, in 2016 on the topic of novel processing technologies for Fiber Bragg grating sensors in composite materials.

Further research work involves the postdoctoral positions with Vrije Universiteit Brussel and Ghent University, Ghent, Belgium, mostly related to integrity assessment methods for composite materials. He joined the nondestructive testing (NDT) Team, ENGIE Laborelec, Linkebeek, Belgium, in January 2019. Besides a versatile activity in site inspections [ultrasonic testing (UT), phased array (PA), eddy current testing (ET)], other activities involve research and development on NDT methods (Thermography, total focusing method (TFM), PA, Hyperspectral, X-Ray computed tomography (CT), etc) for advanced damage detection of materials and work on robotized NDT inspection for application in aerospace, energy or quality evaluation of materials produced with additive manufacturing.

**Paul Scheunders** (Senior Member, IEEE) received the M.S. and Ph.D. degrees in physics with work in the field of statistical mechanics from the University of Antwerp, Antwerp, Belgium, in 1986 and 1990, respectively.

In 1991, he became a Research Associate with Vision Laboratory, Department of Physics, University of Antwerp, where he is a full professor. He has published over 200 articles in international journals and proceedings in the field of image processing, pattern recognition, and remote sensing. His research interests include remote sensing and hyperspectral image (HSI) processing.

Dr. Scheunders is a Senior Member of the IEEE Geoscience and Remote Sensing Society. He has served as a Program Committee Member in numerous international conferences. He is an Associate Editor of the IEEE TRANSACTIONS ON GEOSCIENCE AND REMOTE SENSING.